Key Points:
- Solar wind parameter statistics change with solar cycle phase while preserving PDF functional form
- Solar wind ϵ changes in a manner distinct from other coupling parameters
- Results are independent of PDF functional form

Supporting Information:
- Figure S1
- Figure S2
- Figure S3
- Supporting Information S1

Correspondence to:
E. Tindale,
l.tindale@warwick.ac.uk

Solar cycle variation of the statistical distribution of the solar wind ϵ parameter and its constituent variables

E. Tindale[1] and S. C. Chapman[1]

[1]CFSA, Physics Department, University of Warwick, Warwick, UK

Abstract We use 20 years of Wind solar wind observations to investigate the solar cycle variation of the solar wind driving of the magnetosphere. For the first time, we use generalized quantile-quantile plots to compare the statistical distribution of four commonly used solar wind coupling parameters, Poynting flux, B^2, the ϵ parameter, and vB, between the maxima and minima of solar cycles 23 and 24. We find the distribution is multicomponent and has the same functional form at all solar cycle phases; the change in distribution is captured by a simple transformation of variables for each component. The ϵ parameter is less sensitive than its constituent variables to changes in the distribution of extreme values between successive solar maxima. The quiet minimum of cycle 23 manifests only in lower extreme values, while cycle 24 was less active across the full distribution range.

1. Introduction

The 11 year solar cycle is variable, with an extended minimum observed in cycle 23 and a notably quiet maximum in the most recent cycle 24 [*Lockwood*, 2013; *Zerbo and Richardson*, 2015]. Satellites in the solar wind upstream of Earth provide a comprehensive data set covering several solar cycles. Variables observed in situ are combined into solar wind parameters that aim to capture the driving of the magnetosphere by the solar wind [e.g., *Gonzales*, 1990]. This letter focuses on the systematic changes in the statistical distributions of these solar wind parameters between different phases of the solar cycle.

The Poynting flux S is the energy flux density carried by the electromagnetic fields of the solar wind plasma. Along with S, we will consider three of the most commonly used parameters: the ϵ parameter [*Perreault and Akasofu*, 1978], in which S is scaled to account for energy transport into the magnetosphere [*Koskinen and Tanskanen*, 2002]; the westward electric field, estimated as $v_x B_z$ [*Burton et al.*, 1975]; and finally, B^2, found to be more closely related to solar activity [*Kiyani et al.*, 2007].

There has been extensive work on the statistics of solar wind variables. Early work [*Burlaga and King*, 1979] identified an approximately lognormal probability density function (PDF) of the magnetic field strength. *Feynman and Ruzmaikin* [1994] showed that the PDF of the interplanetary magnetic field (IMF) field strength could not be exactly lognormal due to nonzero kurtosis, which was substantiated later by *Burlaga and Ness* [1996] who determined the PDF to be lognormal with an exponential tail but also discussed the possibility of a Pareto tail. *Koons* [2001] successfully fitted the Gumbel class of extreme value distribution to annual maxima of the 60 MeV proton flux. *Moloney and Davidsen* [2010] found that the block maxima of the ϵ parameter follow the Fréchet distribution; however, this fit overestimated the highest values. Since the Fréchet class is the limiting distribution for a variable that has a PDF with a power law tail [*Schumann et al.*, 2012], a Fréchet fit to block maxima of the ϵ parameter would support Burlaga's earlier proposal of a lognormal PDF with a Pareto tail. *Burlaga and Lazarus* [2000] also found evidence for lognormal distributions of the solar wind speed, density, and temperature, and that these distributions vary with the phase of the cycle. They attributed this variation to the dominance of corotating streams in the solar wind at solar minimum [*Tsurutani et al.*, 2006]. Common to all these findings is the multicomponent nature of PDFs of solar wind variables.

A complementary approach to the statistical analysis of solar wind variables is the use of bursts. These are defined as the integrated signal over periods where the variable continuously exceeds a given threshold; they have been used to compare the solar wind with both solar flares [*Moloney and Davidsen*, 2011] and geomagnetic indices [*Freeman et al.*, 2000a]. The PDFs of burst lifetimes of ϵ, $(v_x B_z)_s$, B^2, and S have all been found

to be power law with an exponential roll off [*Wanliss and Weygand*, 2007; *Freeman et al.*, 2000b], as has the distribution of waiting times of bursts in $B_{z,S}$ [*D'Amicis et al.*, 2006]. Of these fits, *Wanliss and Weygand* [2007] found the power law exponents of the ϵ and $(v_xB_z)_S$ distributions to be solar cycle dependent; however, when looking at higher thresholds, *Moloney and Davidsen* [2014] found no such dependency. In the related studies of geomagnetic indices, *Freeman et al.* [2000a] found the distribution of burst lifetimes of *AU* and *AL* to be multicomponent, including a power law and exponential cutoff similar to ϵ, and *Hush et al.* [2015] found a multicomponent distribution of *AE* burst size, including a solar cycle-dependent exponential component at extreme values.

While these studies have been successful in fitting parts of the distribution of solar wind parameters, there are still open questions, including how the PDF changes over the solar cycle and which of the constituent variables within a parameter such as ϵ drives these changes. In this paper, we address these questions, with the first application of quantile-quantile (QQ) plots [*Gilchrist*, 2000] to the comparison of observed distributions of each solar wind parameter measured at different phases of the solar cycle. We examine the changes in the cumulative distribution functions (CDFs) of the coupling parameters S, B^2, ϵ, and $(v_xB_z)_S$ in cycles 23 and 24, between each maximum and minimum, between successive maxima, and between successive minima. In each case the distribution is multicomponent, and we find that over a broad range each subcomponent has a functional form that remains unchanged across all phases of the solar cycle. The change in CDF, and hence PDF, is captured by a transformation of variables for each subcomponent; this transformation takes the form of $P(x) \rightarrow P(\alpha x + \beta)$, independent of the underlying PDF functional form. Our results quantify the effect of the quiet minimum of solar cycle 23 and the quiet maximum of cycle 24 on the likelihood of observed values of these parameters. We see systematic changes in the PDFs of the constituent variables of ϵ and identify which variable drives the variation in the statistics of ϵ. We find that the statistics of ϵ can be less sensitive to these changes than those of its constituent variables.

In section 2 we introduce the data set and solar wind parameters. In section 3 we describe the QQ plot method and apply it to the solar wind Poynting flux. In section 4 we repeat this analysis for parameters B^2, solar wind ϵ, B_z and v_xB_z, and for all parameters across the full solar cycles. We conclude in section 5.

2. Data

Data from the Magnetic Fields Investigation and Solar Wind Experiment on the Wind spacecraft were provided by National Aeronautics and Space Administration/Goddard Space Flight Center (NASA/GSFC's) OMNI data set. Data were only taken at those times when the spacecraft was situated in the upstream solar wind. During preprocessing, the 15 s cadence interplanetary magnetic field (IMF) and 92 s ion plasma velocity are interpolated to 1 min resolution. The plasma velocity measurements include both fast and slow streams, and all measurements are in geocentric solar magnetospheric (GSM) coordinates. One year of data was taken spanning each of the minima and maxima of cycle 23 and cycle 24, using inclusive dates December 1995 to November 1996 (cycle 23 minimum), October 1999 to September 2000 (cycle 23 maximum), August 2007 to July 2008 (cycle 24 minimum), and November 2013 to October 2014 (cycle 24 maximum). Data gaps are reasonably evenly distributed between successive maxima and minima; they typically cover ∼10% of the data, ranging from ∼5% for the minimum of solar cycle 24 to ∼26% for the maximum of cycle 23. The remaining sample sizes are of order 400,000 samples in each data set. The Wind satellite orbits *L*1 and is, for our yearlong samples at maxima and minima, within 100 R_E of the Sun-Earth line. It is outside this range for ∼8% of the full data set.

The Poynting flux, *S*, is the characteristic energy flux carried by the solar wind. For ideal magnetohydrodynamics, the electric field is $\mathbf{E} = -\mathbf{v} \times \mathbf{B}$, so that the component of Poynting flux along the Sun-Earth line is approximated by

$$S = -\frac{1}{\mu_0} v_x \left(B_y^2 + B_z^2 \right). \tag{1}$$

The ϵ parameter is based on the Poynting flux but is scaled to account for the interaction between the solar wind and magnetosphere. In SI units it is

$$\epsilon = \frac{4\pi}{\mu_0} v B_S^2 \sin^4 \left(\frac{\theta}{2} \right) l_0^2, \tag{2}$$

where v is the ion plasma speed, B_S is the magnitude of the IMF with southward B_z, l_0 is a length scale taken to be 7 R_E, and $\theta = \tan^{-1}(B_y/B_z)$ is the clock angle. The ϵ parameter depends on all three components of the IMF, while the Poynting flux depends on B_y and B_z only.

Energy transfer between solar wind and the magnetosphere is in part ordered by the flux of southward directed IMF (i.e., negative B_z in GSM), due to the increased rate of magnetospheric reconnection. We therefore calculate the solar wind parameters S and B^2 for both the full data set and the subset of data where $B_z < 0$ and the magnetosphere coupling parameters ϵ and $v_x B_z$ at times of southward IMF only. After removing the northward IMF values, the southward IMF subsets of data contained approximately 200,000 data points. The subscript S will denote the southward IMF only subsets of each parameter.

3. QQ Plots for Poynting Flux

The quantile-quantile (QQ) plot is a tool for comparing two statistical distributions. The distribution of an independently and identically (iid) random variable X can be described both by its probability density function (PDF), $P(x)$, and the corresponding cumulative density function (CDF), $C(x)$, which are related via

$$P(x) = \frac{dC(x)}{dx} \tag{3}$$

so that $C(x)$ is the likelihood that the value of variable X will occur below a value x ($X \leq x$). The CDF can be inverted, so that for any likelihood q, a value $x(q)$ can be calculated such that the likelihood of a measurement of X occurring below $x(q)$ is q. The value $x(q)$ is referred to as the qth quantile of the distribution of variable X; for example, the $q = 0.5$ quantile of the distribution, $x(0.5)$, is the median: the value below which 50% of the data lie.

Consider two iid random variables, X_1 and X_2, distributed according to PDFs $P_1(x_1)$ and $P_2(x_2)$ with corresponding CDFs $C_1(x_1)$ and $C_2(x_2)$. The quantiles of the two distributions are as follows:

$$x_1(q_1) = C_1^{-1}(q_1)$$
$$x_2(q_2) = C_2^{-1}(q_2) \tag{4}$$

where $C^{-1}(q)$ is the inverse of CDF $C(x(q))$. The QQ plot then has as its coordinates the quantiles $x_1(q)$ and $x_2(q)$, where the likelihood q is a parametric coordinate. If X_1 and X_2 have same distribution, their quantiles will be the same, and so a straight "$y = x$" line of gradient 1 will be recovered. Any other straight line on the QQ plot would be described by

$$x_2(q) = \alpha x_1(q) + \beta, \tag{5}$$

in which case the CDFs are related by a transformation of variables:

$$C_2(x) = C_1\left(\frac{x - \beta}{\alpha}\right). \tag{6}$$

With equation (3) this yields

$$P_2(x) = \frac{1}{\alpha}P_1\left(\frac{x - \beta}{\alpha}\right), \tag{7}$$

so that the corresponding PDFs are related by the same transformation of variables. The scaling parameter α preserves the normalization, so that the integrated PDF is unity. Hence, if the QQ plot is linear, the functional form of the underlying PDF of both variables X_1 and X_2 is the same, subject to a transformation of variables from x to $(x - \beta)/\alpha$. The parameter α denotes a change in scale, while β is a shift in location. A positive β value indicates an increase in mean, so that the likelihood of large values of X increases as the whole PDF is shifted. If $\alpha > 1$, a given likelihood q corresponds to a larger value of X, resulting in the stretching of the PDF tail. This in turn modifies the raw higher moments of the distribution; however, the standard measures of skewness and kurtosis can be normalized to account for the change in scale [*Gilchrist*, 2000]. Both α and β can be found from the data with a linear regression to the QQ plot.

Figure 1 shows QQ plots comparing the distributions of Poynting flux, B^2, ϵ and vB between solar cycle phases; in the left column we compare the minimum of cycle 23 to that of cycle 24, in the central column we compare
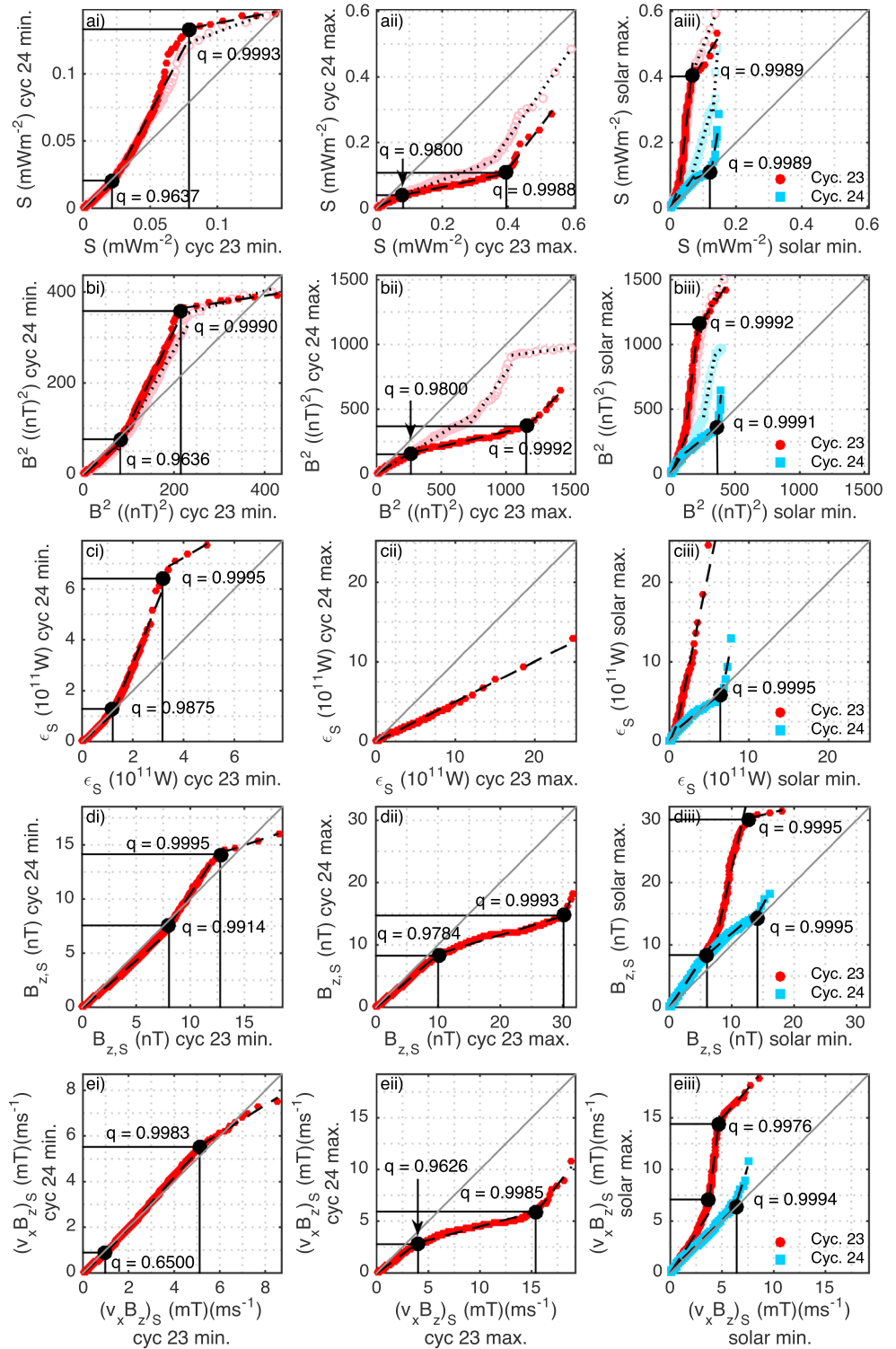
Figure 1. QQ plots for (ai–aiii) solar wind Poynting flux, (bi–biii) B^2, (ci–ciii) the ϵ_S parameter, (di–diii) $B_{z,S}$, and (ei–eiii) $(v_x B_z)_S$, comparing the quantiles of the minimum of solar cycle 24 (ordinate) with the minimum of cycle 23 (abscissa) (column i); the maximum of solar cycle 24 (ordinate) with the maximum of cycle 23 (abscissa) (column ii); and the solar maximum (ordinate) with the solar minimum (abscissa) for both cycle 23 (red) and cycle 24 (blue) (column iii). Open pink circles (and open light blue squares) are quantiles of the full data set, and filled red circles (filled dark blue squares) are quantiles when the IMF is southward. Black dashed lines show least squares linear regressions with fitting ranges shown by black solid lines. The parameters of these fits are given in Table S1 in the supporting information.

the successive maxima, and in the right column we compare each cycle's maximum to its minimum. In each case we compare the 0.0001 to 0.9999 quantiles. A plot in the same format is given for additional quantities in the supporting information, along with a discussion of uncertainties.

Figures 1ai–1aiii show the results for the solar wind Poynting flux. In each case the QQ plots are multicomponent, with three approximately linear regions. A linear region of the QQ plot indicates that the functional form of the PDF in that region does not change; thus, a transformation of variables captures how the distribution is changing over the solar cycle, as described above. These ranges are indicated on the plots. We perform a three-component linear-piecewise fit to these plots. The R^2 statistic associated with the each linear fit (given in Tables S1–S3 in the supporting information) exceeds 0.9 in almost all cases, indicating that the linear transformations provide a good representation of the change in distribution.

The QQ plot of Poynting flux with southward IMF, S_S, comparing successive minima (Figure 1ai) consists of three such approximately linear regions: a "bulk component," containing data in the 0 to 0.9637 quantiles; a "high component" spanning the 0.9637 to 0.9993 quantiles; and an "extreme component," which includes values above the 0.9993 quantile. The bulk component has an α value of 0.864(2), where the error denotes the 95% confidence interval of the value, and a β close to zero. This component of the distribution thus shows a small change in scale between the two minima, so that its PDF essentially does not change. The high component has a significant change in scale of $\alpha = 1.90(3)$, as well as a shift in location of $\beta = -0.0237(11)$. Finally, the extreme component undergoes a transformation of $S_{S,24} = 0.197(45)S_{S,23} + 0.118(5)$, showing a decrease in the scale of these values, but a large (∼10%) increase in their mean. The high and extreme components appear above the $y = x$ reference line, so that the increased activity of the minimum of cycle 24 relative to cycle 23 is manifest mainly in these extreme values, rather than in the bulk of the distribution.

Conversely, we can see that in Figure 1aii the quantiles all lie below the $y = x$ line, so that the maximum of cycle 24 was significantly less active than the maximum of cycle 23. Again, the QQ plot can be divided into linear regions which we denote as bulk, high, and extreme components. These linear relationships again indicate that within each of the components of the underlying PDF, the functional form is the same at both solar maxima. The crossover points between these regions of the CDF occur at $q = 0.9800$ and $q = 0.9988$. Unlike the change between successive minima, the bulk component of the distribution changes scale significantly between the successive maxima, with $\alpha = 0.545(1)$. The location of the bulk component does not change. The transformation of variables for the high component was $S_{S,24} = 0.209(2)S_{S,23} + 0.0231(4)$ and for the extreme component was $S_{S,24} = 1.32(20)S_{S,23} - 0.409(88)$. The high component of the PDF therefore decreases in scale but slightly increases in mean, while the opposite is true for the extreme component. We repeated this analysis comparing the full 11 year data sets of cycles 23 and 24 (see supporting information) and find that cycle 23 is overall more active.

Between the successive maxima, the translations of the high and extreme components are sensitive to whether the full data set or the southward IMF subset is included in the CDF. The bulk component undergoes approximately the same transformation of variables in both cases. The change of scale α of the high component increases from $\alpha = 0.209(2)$ for S_S to $\alpha = 0.366(5)$, while for the extreme component α is roughly the same, changing from $\alpha = 1.32(20)$ to $\alpha = 1.42(10)$. The shift in location β is ∼50% smaller for the high component and ∼20% larger for the extreme component, once the northward IMF values of S are included. The QQ plot thus has three well-defined linear components that translate according to equation (5) between phases of the solar cycle, irrespective of whether or not northward IMF values are included. However, the changes in scale and location (α and β) of the underlying PDF are more pronounced if we only consider the southward IMF subset.

Figure 1aiii compares the distribution of Poynting flux at the maximum and minimum of each cycle. Again, the QQ plot is composed of several approximately linear regions, indicating the multicomponent and invariant functional form of the PDF discussed above. For both solar cycles, the bulk component occurs close to the origin, so that on this scale the QQ plots appear to show only the high and extreme components. These components again undergo a simple translation (as in equation (5)) between solar minimum and maximum; however, the transformations are different for the two cycles. In cycle 23, the high component has a large change in scale of $\alpha = 9.18(17)$, while the extreme component shifts in location, $\beta = 0.291(31)$ but has a smaller change in scale ($\alpha = 1.57(32)$). For cycle 24, the high component remains closer to the $y = x$ line ($\alpha = 0.422(46)$, $\beta = 0.0587(43)$) and so shows a less pronounced change between solar maximum and minimum. The extreme component does have a significant transformation, with both a large change of

scale $\alpha = 5.90 \pm 1.98$ and large shift in location $\beta = -0.618(266)$. Therefore, the quietness of cycle 24 is manifest in the bulk and high components, which are the same at maximum and minimum; only the extreme values above the $q = 0.9989$ quantile show increased likelihood at maximum relative to the cycle minimum.

4. QQ Plots for B^2, ϵ_S, $B_{z,S}$, and $(v_x B_z)_S$

Figures 1bi–1biii through 1ei–1eiii plot the above solar cycle phase comparisons for the B^2, $B_{z,S}$, ϵ_S, and $(v_x B_z)_S$ parameters, with the latter three calculated using only values with southward IMF. The QQ plots can again be split into multiple approximately linear components, with R^2 values consistently above 0.9, so that the PDF functional form is approximately invariant for all parameters; it, again, simply translates as in equation (5).

Quantiles of both the full and southward IMF only B^2 data sets are shown in Figures 1bi–1biii. Qualitatively, these panels show the same behavior as in Figures 1ai–1aiii, indicating that S simply tracks B^2. In all three plots, the transitions between components occur at similar quantiles for both B_S^2 and S_S. However, although the trends are the same, the α and β parameters differ between S_S and B^2, suggesting that the solar wind speed does not affect the form of the transformations but does alter the details. The comparison of the solar maxima (Figure 1bii) also shows the same sensitivity as the Poynting flux to whether all values or the southward IMF only subset is used.

Between successive solar minima, the QQ plot for ϵ_S (Figure 1ci) is qualitatively similar to those of S_S and B_S^2 (Figures 1ai and 1bi). However, when we consider how the distribution translates between successive solar maxima (Figure 1cii) the distribution of the ϵ_S parameter transforms in a remarkably different way to the other variables. The PDF retains its functional form and is translated by a single change in scale over the full range. The α value of this transformation is 0.501(1), which is similar to the α values of the bulk components of the S_S and B_S^2. The high and extreme values of ϵ_S thus do not retain the distinct changes between successive maxima seen in S_S and B_S^2. Similar behavior of ϵ_S is found when comparing the maximum and minimum of cycle 23 in Figure 1ciii; that is, the high and extreme components are indistinguishable and translate with a single change of scale $\alpha = 4.81(9)$. Now, ϵ depends upon all three components of magnetic field, whereas the Poynting flux depends on the y and z components only; ϵ also includes a factor that depends on the clock angle. In Figure S1, we plot, in the same format as Figure 1, the changes in B_x^2 and $B_{yz}^2 = B_y^2 + B_z^2$, along with the clock angle contribution to ϵ. We see that the distribution of the clock angle contribution does not change between the different phases of the solar cycles; therefore, this does not explain the relative insensitivity of ϵ. However, the distributions of B_x^2 and B_{yz}^2 translate in opposite directions on the plot; for example, the extreme components have $\alpha < 1$ and $\alpha > 1$, respectively (values are $\alpha = 0.0602(408)$ and $\alpha = 1.50(20)$). When these are combined within a single parameter, they may tend to suppress these changes. We have repeated this analysis (see supporting information) for the Milan and Newell coupling parameters [*Milan et al.*, 2008; *Newell et al.*, 2007] and find that they are intermediate in sensitivity between ϵ and Poynting flux. In common with the Poynting flux, they only depend on the y and z components of the IMF.

Within Figures 1di–1diii and 1ei–1eiii, the distributions of variables $B_{z,S}$ and $(v_x B_z)_S$ show little change between the two minima except at the extreme values (Figures 1di and 1ei), with less sharp transitions between components. The comparison of the maxima for these variables (Figures 1dii and 1eii) shows three linear components, but again with less clear transitions; this is reflected in the lower R^2 values, which are 0.9722 and 0.9670 for the high component of $B_{z,S}$ and $(v_x B_z)_S$, respectively, compared to 0.9938 and 0.9829 for S_S and B_S^2. The similarity of the QQ plots for $B_{z,S}$ and $(v_x B_z)_S$ again suggests that the magnetic field drives the variation of the distribution of the constructed parameters. The solar wind speed also contributes to the change in distribution between the maximum and minimum of cycle 24: compare Figures 1diii and 1eiii with Figure S1aiii in the supporting information.

In Figures 1aiii, 1biii, and 1ciii we see similar qualitative behavior across the parameters. The bulk and high components of the cycle 24 QQ plot are close to the $y = x$ line in most cases, indicating that the distribution of each variable for cycle 24 was the same at maximum and minimum up to the highest quantiles. The outstanding case is in Figure 1diii, where the bulk component of the $B_{z,S}$ distribution transforms in the same manner for both cycle 23 and 24, up to the $q = 0.9800$. The relatively low activity of cycle 24 is also evident; for all variables, the quantiles of cycle 24 lie below those of cycle 23. The extreme component occurs between $q = 0.9989$ and $q = 0.9995$ for all variables in cycle 24, and all except ϵ_S and $(v_x B_z)_S$ in cycle 23, suggesting that in all these variables (with the exception of ϵ_S) there is an extreme tail which transforms differently to the rest of the distribution.

Finally, we compared the distributions of the two full cycles; see the supporting information for QQ plots and a detailed discussion. Overall, cycle 23 shows higher activity, despite its quiet minimum. For all four parameters, ranges are again found over which the QQ plots are linear, suggesting that the transformation of variables in equation (5) captures the change in the PDF.

5. Summary

We investigated how the probability density functions of four solar wind-magnetosphere coupling parameters change over the two most recent solar cycles using quantile-quantile plots. The distributions for Poynting flux, B^2, ϵ_S and the westward electric field $(v_x B_z)_S$ were compared between cycle 23 minimum and cycle 24 minimum, between cycle 23 maximum and cycle 24 maximum, and between the maximum and minimum of each of cycles 23 and 24.

We found that for all parameters the PDF has a multicomponent functional form which does not change over the solar cycle or between cycles. Instead, a linear transformation of variables for each component is required to map that region of the PDF from one solar cycle phase to another. These transformations can be found by fitting least squares regressions to linear regions of the QQ plot. We identified three regions of the distributions in the QQ plots; the bulk component, up to $q \sim 0.96$, and beyond this the high and extreme components. The bulk component undergoes a change in scale between solar maxima but is roughly the same at both minima. The high and extreme components for S, B^2 and $(v_x B_z)_S$ are each associated with a unique change in both scale and location. The ϵ_S parameter behaves differently to S_S, B_S^2 and $(v_x B_z)_S$ as the change in its PDF between successive maxima is captured by a single change in scale over the full range, so the high and extreme values are insensitive to the changes in their distribution seen in S_S and B_S^2.

The QQ plots for S resemble those of B^2, and likewise the QQ plots for $(v_x B_z)_S$ track those of $B_{z,S}$, implying that changes in B drive changes in the PDFs of the solar wind coupling parameters. Cycle 23 exhibited a quieter minimum than cycle 24, which is manifest in the distribution as larger amplitude (quantile) high and extreme components at the minimum of cycle 24 than cycle 23, while the bulk component was roughly the same for both minima. The overall activity of cycle 23 was higher than that of cycle 24, seen across the distribution at the maximum of cycle 23 compared to the maximum of cycle 24. The changes in the distribution of S and B^2 between successive maxima were also found to be more pronounced in the distribution of values when IMF is southward.

As the functional form of the distribution of each solar wind variable does not change between extrema of cycles 23 and 24, it could be an intrinsic property, and as such would remain the same in future cycles. This qualitative property of the full distribution provides a benchmark for models and may support prediction of the likelihood of extreme space weather events. However, as we have shown, this depends on the variable chosen, as the ϵ parameter is less sensitive to changes in the likelihood of its large values than the S, B^2 and $(v_x B_z)_S$ variables.

References

Burlaga, L. F., and J. H. King (1979), Intense interplanetary magnetic fields observed by geocentric spacecraft during 1969-1975, *J. Geophys. Res.*, *84*(A11), 6633–6640, doi:10.1029/JA084iA11p06633.

Burlaga, L. F., and A. J. Lazarus (2000), Lognormal distributions and spectra of solar wind plasma fluctuations: Wind 1995–1998, *J. Geophys. Res.*, *105*(A2), 2357–2364, doi:10.1029/1999JA900442.

Burlaga, L. F., and N. F. Ness (1996), Magnetic fields in the distant heliosphere approaching solar minimum: Voyager 1 and 2 observations during 1994, *J. Geophys. Res.*, *101*(A6), 13,473–13,481, doi:10.1029/96JA00523.

Burton, R. K., R. L. McPherron, and C. T. Russell (1975), An empirical relationship between interplanetary conditions and *Dst*, *J. Geophys. Res.*, *80*(31), 4204–4214, doi:10.1029/JA080i031p04204.

D'Amicis, R., R. Bruno, B. Bavassano, V. Carbone, and L. Sorriso-Valvo (2006), On the scaling of waiting-time distributions of the negative IMF B_z component, *Ann. Geophys.*, *24*, 2735–2741, doi:10.5194/angeo-24-2735-2006.

Feynman, J., and A. Ruzmaikin (1994), Distributions of the interplanetary magnetic field revisited, *J. Geophys Res.*, *99*(A9), 17,645–17,651, doi:10.1029/94JA01098.

Freeman, M. P., N. W. Watkins, and D. J. Riley (2000a), Evidence for a solar wind origin of the power law burst lifetime distribution of the *AE* indices, *Geophys. Res. Lett.*, *27*(8), 1087–1090, doi:10.1029/1999GL010742.

Freeman, M. P., N. W. Watkins, and D. J. Riley (2000b), Power law distributions of burst duration and interburst interval in the solar wind: Turbulence or dissipative self-organized criticality?, *Phys. Rev. E*, *62*(6), 8794–8797, doi:10.1103/PhysRevE.62.8794.

Gilchrist, W. G. (2000), *Statistical Modelling With Quantile Functions*, Chapman and Hall, Fla.

Gonzales, W. D. (1990), A unified view of solar wind-magnetosphere coupling functions, *Planet. Space. Sci.*, *38*(5), 627–632, doi:10.1016/0032-0633(90)90068-2.

Hush, P., S. C. Chapman, M. W. Dunlop, and N. W. Watkins (2015), Robust statistical properties of the size of large burst events in *AE*, *Geophys. Res. Lett.*, *42*, 9197–9202, doi:10.1002/2015GL066277.

Kiyani, K., S. C. Chapman, B. Hnat, and R. M. Nicol (2007), Self-similar signature of the active solar corona within the inertial range of solar-wind turbulence, *Phys. Rev. Lett.*, *98*, 211101, doi:10.1103/PhysRevLett.98.211101.

Koons, H. C. (2001), Statistical analysis of extreme values in space science, *J. Geophys. Res.*, *106*(A6), 10,915–10,921, doi:10.1029/2000JA000234.

Koskinen, H. E., and E. I. Tanskanen (2002), Magnetospheric energy budget and the epsilon parameter, *J. Geophys. Res.*, *107*(A11), 1415, doi:10.1029/2002JA009283.

Lockwood, M. (2013), Reconstruction and prediction of variations in the open solar magnetic flux and interplanetary conditions, *Living Rev. Sol. Phys.*, *10*, 4. [Available at http://www.livingreviews.org/lrsp-2014-4, (accessed 16/02/16).]

Milan, S. E., P. D. Boakes, and B. Hubert (2008), Response of the expanding/contracting polar cap to weak and strong solar wind driving: Implications for substorm onset, *J. Geophys. Res.*, *113*, A09215, doi:10.1029/2008JA013340.

Moloney, N. R., and J. Davidsen (2010), Extreme value statistics in the solar wind: An application to correlated Levy processes, *J. Geophys. Res.*, *115*, A10114, doi:10.1029/2009JA015114.

Moloney, N. R., and J. Davidsen (2011), Extreme bursts in the solar wind, *Geophys. Res. Lett.*, *38*, L14111, doi:10.1029/2011GL048245.

Moloney, N. R., and J. Davidsen (2014), Stationarity of extreme bursts in the solar wind, *Phys. Rev. E*, *89*, 052812, doi:10.1103/PhysRevE.89.052812.

Newell, P. T., T. Sotirelis, K. Liou, C.-I. Meng, and F. J. Rich (2007), A nearly universal solar wind-magnetosphere coupling function inferred from 10 magnetospheric state variables, *J. Geophys. Res.*, *112*, A01206, doi:10.1029/2006JA012015.

Perreault, P., and S.-I. Akasofu (1978), A study of geomagnetic storms, *Geophys. J. R. Astron. Soc.*, *54*(3), 547–573, doi:10.1111/j.1365-246X.1978.tb05494.x.

Schumann, A. Y., N. R. Moloney, and J. Davidsen (2012), Extreme value and record statistics in heavy-tailed processes with long-range memory, in *Extreme Events and Natural Hazards: The Complexity Perspective*, edited by A. S. Sharma, AGU, Washington, D. C., doi:10.1029/2011GM001088.

Tsurutani, B. T., et al. (2006), Corotating solar wind streams and recurrent geomagnetic activity: A review, *J. Geophys Res.*, *111*, A07S01, doi:10.1029/2005JA011273.

Wanliss, J. A., and J. M. Weygand (2007), Power law burst lifetime distribution of the *SYM-H* index, *Geophys. Rev. Lett.*, *34*, L04107, doi:10.1029/2006GL028235.

Zerbo, J.-L., and J. D. Richardson (2015), The solar wind during current and past solar minima and maxima, *J. Geophys. Res. Space Physics*, *120*, 10,250–10,256, doi:10.1002/2015JA021407.

Supporting Information for "Solar cycle variation of the statistical distribution of the solar wind ϵ parameter and its constituent variables"

E. Tindale[1], and S.C. Chapman[1]

Contents of this file

Introduction

This supporting information contains the additional quantile-quantile (QQ) plots referred to in the main text. In figure S1 we compare, in the same format as figure 1, the distributions of the solar wind speed v; the clock angle contribution to ϵ, $\sin^4(\theta/2)$; the x and transverse components of B^2; and the Milan and Newell coupling parameters, ϕ_D and $d\phi/dt$, between different phases of solar cycle 23 and 24. The construction of these plots and their results is discussed in section S1. To compare the full cycle 23 to full cycle 24, we took data spanning 10 years for each cycle, and calculated the resultant distributions for each of the previously discussed variables. The QQ plots comparing the full cycles are shown in figure S2, and discussed in section S2. Tables S1, S2 and S3 provide the parameters of the linear fits shown by black dashed lines in figures 1 (main text), S1 and S2 respectively, alongside the valid fitting range and the R^2 statistic for each regression. Finally, in section S3 we briefly discuss the quantification of uncertainties involved in the QQ plot method.

S1. QQ plots for v, $\sin^4(\theta/2)$, B_x^2, $B_{y,z}^2$, ϕ_D and $d\phi/dt$,

In the main text, we see the change in the distribution of the ϵ parameter between successive solar maxima took a different form to the changes in the distributions of the magnetic energy density and the Poynting flux. We now repeat the analysis for constituent parameters v, $sin^4(\theta/2)$, B_x^2, and $B_{y,z}^2$ to gain further insight into this result, and the Milan and Newell coupling parameters [*Milan et al.*, 2008; *Newell et al.*, 2007] to determine whether the behaviour is unique to ϵ, or is a characteristic of composite coupling parameters. The Milan and Newell parameters are

$$\phi_D = L_{eff} v_x B_{yz} \sin^2(\frac{\theta}{2}) \qquad (1)$$

$$\frac{d\phi}{dt} = v_x^{4/3} B_{yz}^{2/3} \sin^{8/3}(\frac{\theta}{2}) \qquad (2)$$

respectively, where $B_{yz}^2 = B_y^2 + B_z^2$, L_{eff} is a length scale taken to be $2.75R_E$, and θ is the clock angle. The same data were used here as in the main text, and all parameters are calculated only at times of southward IMF.

Figure S1 shows the QQ plots for a) solar wind speed, v; b) $sin^4(\theta/2)$; c) B_x^2; d) $B_{y,z}^2$; e) the Milan parameter, ϕ_D; and f) the Newell parameter, $d\phi/dt$, comparing the distributions between (i) successive minima, (ii) successive maxima, and (iii) each cycle's maximum and its minimum. As in figure 1 of the main letter, these plots can be approximated by linear-piecewise fits, within which a simple transformation of variables captures the change in that region of the distribution.

In panel (aii), the distribution of the velocity changes between solar cycle phases, with three linear components of increasing gradient. As the changes in v qualitatively follow those seen in B^2 (main text, figure 1, row (b)), taken together this would enhance the change in the extreme component of ϵ, rather than suppress it. Row (b) of figure S1 shows that the distribution of the clock angle term does not change either within a solar cycle or between solar cycles. Therefore, it does not contribute to how the distribution of ϵ is changing. Comparing panels (cii) and (dii) however, the high and extreme components for B_x^2 and $B_{y,z}^2$ translate in opposite senses; that is, the high component B_x^2 undergoes a scale change which exceeds unity, while the high α value for the $B_{y,z}^2$ component is less than one, with the reverse being true for the extreme components. When combined, these changes in the distributions of the constituent variables would act to counteract eachother, resulting in lower sensitivity of the ϵ parameter to solar cycle changes. The Poynting flux retains its sensitivity as it is dependent on only the B_y and B_z.

Both the Milan and Newell parameters depend on $B_{y,z}$, and are consistent with the above analysis. In particular, changes to the distribution of ϕ_D (row (e) of figure S1) track the changes seen in row (e) of figure 1 for vB, on which ϕ_D is based. The Newell parameter shows less pronounced changes in its distribution, with no distinction between the bulk and higher components, so its sensitivity is intermediate between that of ϵ and the Poynting flux.

S2. Comparing full 11 year cycles

To compare cycle 23 to cycle 24, 1-minute resolution interplanetary magnetic field (IMF) and plasma velocity data was obtained from the NASA OMNIWeb dataset, from December 1995 to September 2006 for cycle 23 and October 2006 to October 2015 for cycle 24. From these observations, the variables S_S, B_S^2, ϵ_S, $(v_x B_z)_S$, $B_{z,S}$, v_S, $d\phi/dt$, and ϕ_D were calculated. The 0.0001 to 0.9999 quantiles of these 10 year time series were then found and the QQ plots constructed via the method given in section 3 of the main text. The plots are shown in figure S2.

For all eight parameters, all quantiles appear below the "$y = x$" reference line, which indicates that the activity of cycle 23 was overall higher than that of cycle 24, despite its quiet minimum. The multi-component functional form

[1]CFSA, Physics Department, University of Warwick, Warwick, UK

of the PDF is recovered for all four parameters, however for all parameters other than v, the comparisons between full cycles are well approximated by a 2-component linear piecewise fit, as opposed to the three-component structure seen in figure 1 (main text). The "extreme" tail around quantile $q = 0.9990$ in the comparisons between solar cycle phases translates in the same manner as the "high" component for the distributions taken over the full solar cycle. The transitions between the bulk and high regions occur at quantiles between $q = 0.9920$ and $q = 0.9980$ for all parameters.

The bulk component of the PDF transforms in a manner similar to that discussed above for successive solar maxima, with a similar change in scale α and little shift in location β. For each parameter the α value of the bulk component is larger for the comparison of full cycles than for the comparison of successive maxima; for example for Poynting flux S_S, the change of scale between full cycles is $\alpha = 0.587(1)$, compared to $\alpha = 0.545(1)$ between maxima. Distinct from the comparisons between solar maxima, the ϵ_S, $(v_x B_z)_S$, ${}^{d\phi}\!/_{dt}$, and ϕ_D parameters transform in the same manner as S_S and B^2 between cycles 23 and 24.

The high components for S and B^2 are again sensitive to whether the full dataset or southward-IMF values only are used in the distribution. The effect is less pronounced than for the comparisons between successive maxima, manifesting in a $\sim 20\%$ higher change of scale α and a $\sim 15\%$ lower shift in location between the full cycles for the full dataset relative to the southward-IMF only subset.

S3. Quantification of uncertainties

The uncertainty in the QQ plot arises in the sampling of the quantile function. The empirical CDF is calculated by sorting the measured values into ascending order, and plotting each value against the proportion of data it exceeds, creating a 'stepwise' function (see, for example, the dark blue line in figure S3. When this is inverted to calculate the quantile function, it may be necessary to linearly interpolate between two consecutive values of the empirical CDF. The uncertainty on each quantile can then be estimated as the length of the step between the two CDF values.

An example empirical CDF (Poynting flux and the minimum of cycle 23) is shown by the dark blue line in figure S3, alongside inset magnifications of the regions around the $q = 0.5$ and $q = 0.95$ quantiles. The light blue lines show the 95% confidence band, calculated using Greenwood's variance formula [*Cox and Oakes*, 1984]. The confidence intervals are sufficiently small that they can only be seen in the magnified insets; furthermore at all points they exceed the width of each CDF step. This indicates that the error on each quantile, and thus on the QQ plot along both the x and y axes, is small.

References

Cox, D. R., and D. Oakes (1984), *Analysis of survival data*, Chapman and Hall, Florida.

Milan, S. E., P. D. Boakes, and B. Hubert (2008), Response of the expanding/contracting polar cap to weak and strong solar wind driving: Implications for substorm onset, *J. Geophys. Res.*, *113*(A09215), doi:10.1029/2008JA013340.

Newell, P. T., T. Sotirelis, K. Liou, C.-I. Meng, and F. J. Rich (2007), A nearly universal solar wind-magnetosphere coupling function inferred from 10 magnetospheric state variables, *J. Geophys. Res.*, *112*(A01206), doi:10.1029/2006JA012015.
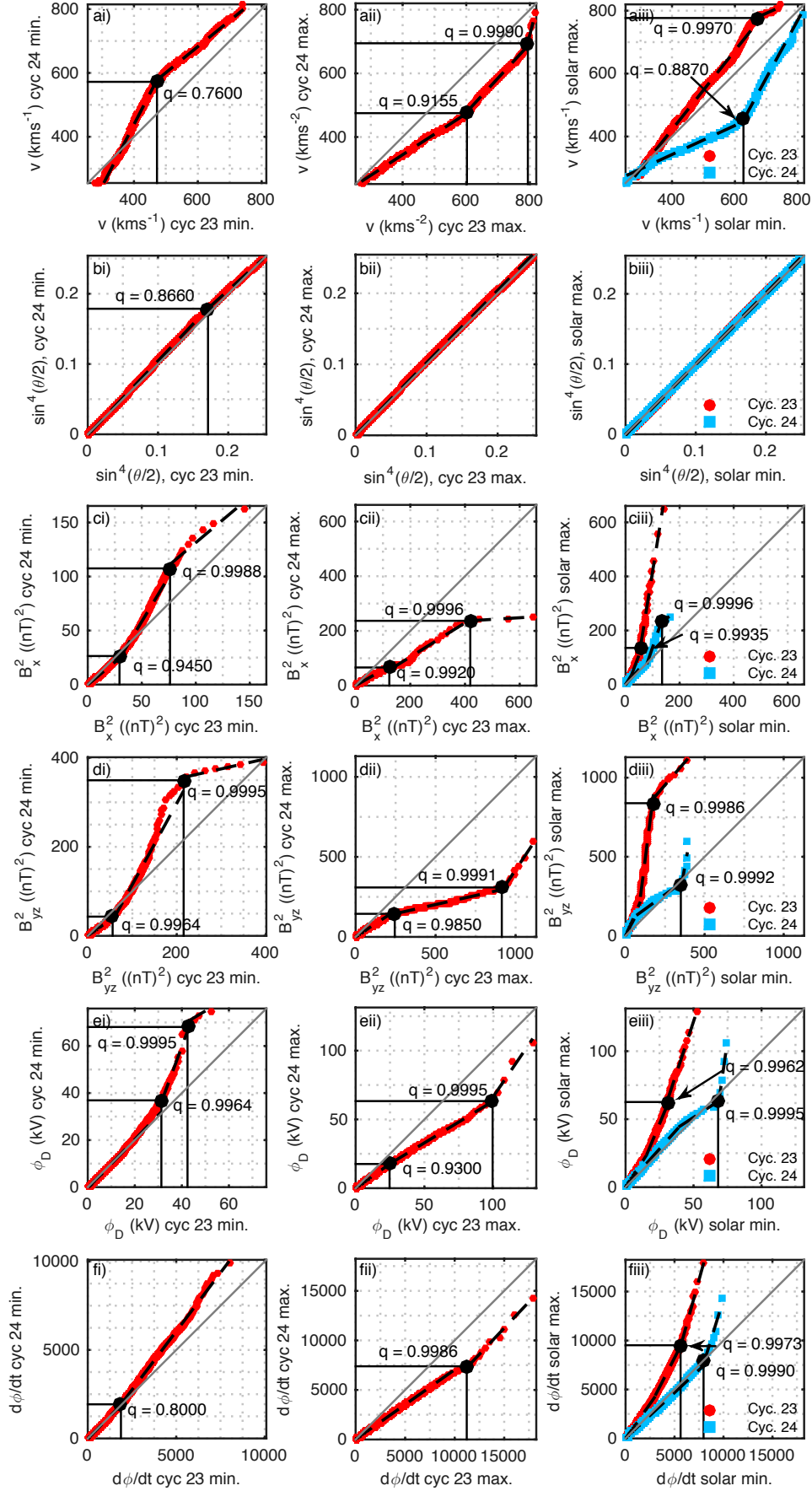
Figure S1: QQ plots comparing the 0.0001 to 0.9999 quantiles of a) solar wind speed, v; b) $sin^4(\theta/2)$; c) B_x^2; d) $B_{y,z}^2$; e) the Milan parameter, ϕ_D; and f) the Newell parameter, $d\phi/dt$ between i) the consecutive solar minima, ii) the solar maxima, and iii) between the maximum and minimum of each of cycles 23 (red) and 24 (blue). Quantiles are calculated from the southward-IMF values. Black dashed lines show the least-squares piecewise linear fits (with fit parameters shown in table S2) defined within the ranges marked by the solid black lines.
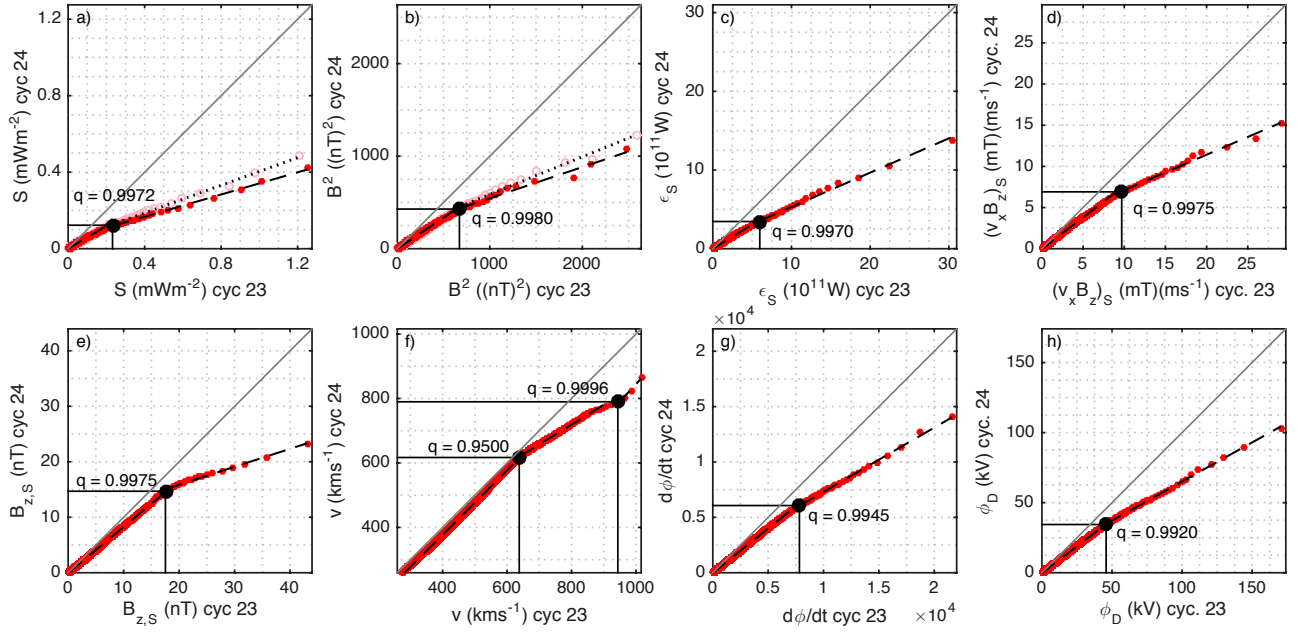
Figure S2: QQ plots for a) Poynting flux, b) B^2, c) ϵ_S, d) $(v_x B_z)_S$, e) $B_{z,S}$, f) solar wind speed v, g) the Newell parameter and h) the Milan parameter, comparing the distribution of each parameter over the full cycle 23 to the distribution over full cycle 24. As in figure 1, open pink circles in panels a) and b) denote the quantiles of the dataset including northward IMF values, filled red circles denote quantiles of the southward-IMF subset. Black dashed lines show the least-squares linear regressions to each component, with parameters given in table S3.
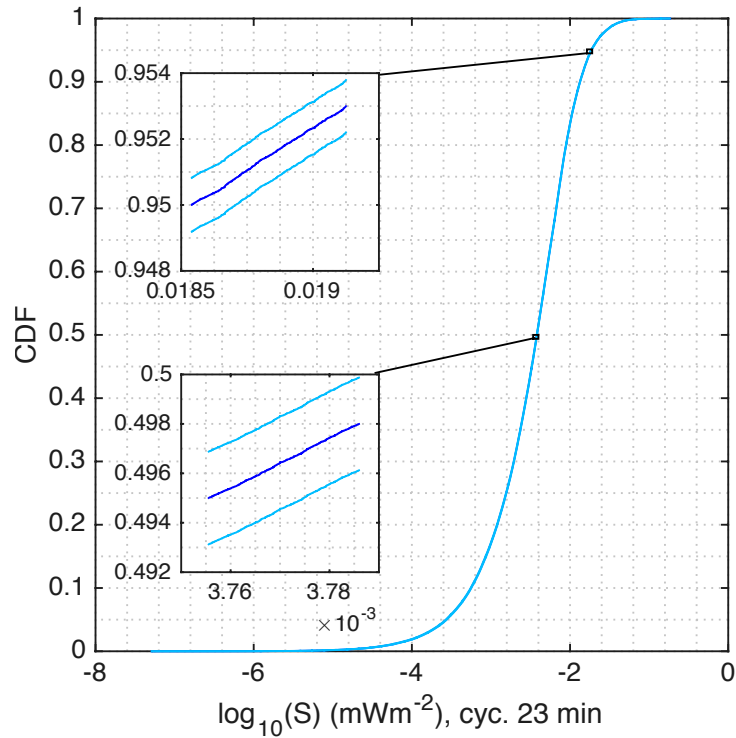
Figure S3: The empirical cumulative distribution function of the Poynting flux, with logarithmic abscissa in the main plot only. 95% confidence intervals, derived using the Greenwood formula, are shown in light blue. Inset are magnifications of the regions around the $q = 0.5$ (lower inset) and $q = 0.95$ (upper inset) quantiles of the CDF.

Table S1: The fit parameters of the linear regressions shown by the black dashed lines in figure 1 (main text). Column 1 gives the label of the relevant panel as shown in figure 1. In column 2, the subscript S denotes usage of the southward-IMF only subset. The third column defines each component in terms of its contribution to the PDF, as discussed in sections 3 and 4 of the main text. Column 4 gives the range of quantiles to which each fit applies. The gradient α and intercept β are given in columns 5 and 6 respectively, with the 95% confidence interval shown in parentheses. Finally, the R^2 value for each fit is included in the 7th column, as an indication of the goodness of fit. * Marked fits have been omitted from the figure for clarity.

| Panel	Parameter	PDF component	Fitting range	α	β	R^2
ai	S_S	Bulk	$0.0001 \to 0.9637$	0.8642(16)	$-3.607(107) \times 10^{-4}$	0.9915
ai	S_S	High	$0.9637 \to 0.9993$	1.896(32)	$-0.0237(11)$	0.9752
ai	S_S	Extreme	$0.9993 \to 0.9999$	0.1965(447)	0.1181(49)	0.9624
ai*	S	Bulk	$0.0001 \to 0.9416$	0.8192(5)	$-3.375(316) \times 10^{-5}$	0.9990
ai*	S	High	$0.9416 \to 0.9994$	1.638(11)	$-0.0156(3)$	0.9937
ai	S	Extreme	$0.9994 \to 0.9999$	0.3753(1044)	0.0934(110)	0.9614
aii	S_S	Bulk	$0.0001 \to 0.9800$	0.5450(13)	$4.486(227) \times 10^{-4}$	0.9857
aii	S_S	High	$0.9800 \to 0.9988$	0.2089(24)	0.0231(4)	0.9938
aii	S_S	Extreme	$0.9988 \to 0.9999$	1.319(202)	$-0.4085(884)$	0.9548
aii*	S	Bulk	$0.0001 \to 0.9800$	0.5685(11)	$3.536(189) \times 10^{-4}$	0.9911
aii	S	High	$0.9800 \to 0.9982$	0.3660(47)	0.0133(8)	0.9925
aii	S	Extreme	$0.9982 \to 0.9999$	1.418(97)	$-0.3548(422)$	0.9838
aiii	S_S, cyc. 23	Bulk	$0.0001 \to 0.9815$	2.475(8)	$-0.0010(1)$	0.9759
aiii	S_S, cyc. 23	High	$0.9815 \to 0.9989$	9.180(168)	$-0.1855(67)$	0.9853
aiii	S_S, cyc. 23	Extreme	$0.9989 \to 0.9999$	1.567(319)	0.2911(31)	0.9319
aiii*	S, cyc. 23	Bulk	$0.0001 \to 0.9790$	2.463(8)	$-9.650(589) \times 10^{-4}$	0.9736
aiii*	S, cyc. 23	High	$0.9790 \to 0.9990$	8.402(108)	$-0.1556(42)$	0.9917
aiii	S, cyc. 23	Extreme	$0.9990 \to 0.9999$	2.563(93)	0.2380(87)	0.9980
aiii	S_S, cyc. 24	Bulk	$0.0001 \to 0.9973$	1.337(3)	0.0012(1)	0.9859
aiii	S_S, cyc. 24	High	$0.9973 \to 0.9989$	0.4218(455)	0.0587(43)	0.9631
aiii	S_S, cyc. 24	Extreme	$0.9989 \to 0.9999$	5.901(1.985)	$-0.6181(2659)$	0.8341
aiii*	S, cyc. 24	Bulk	$0.0001 \to 0.9968$	1.587(1)	$2.941(88) \times 10^{-4}$	0.9989
aiii	S, cyc. 24	High	$0.9968 \to 0.9996$	3.334(82)	$-0.1171(75)$	0.9962
aiii	S, cyc. 24	Extreme	$0.9996 \to 0.9999$	13.45(9.56)	$-1.452(1.308)$	0.9483
bi	B_S^2	Bulk	$0.0001 \to 0.9636$	0.8566(17)	$-2.571(47)$	0.9909
bi	B_S^2	High	$0.9636 \to 0.9990$	2.074(16)	$-99.84(1.79)$	0.9948
bi	B_S^2	Extreme	$0.9990 \to 0.9999$	0.1510(340)	331.5(10.3)	0.9291
bi*	B^2	Bulk	$0.0001 \to 0.9440$	0.7286(10)	$-1.315(32)$	0.9947
bi	B^2	High	$0.9440 \to 0.9991$	1.775(13)	$-82.78(1.40)$	0.9929
bi	B^2	Extreme	$0.9991 \to 0.9999$	0.2926(613)	285.4(18.6)	0.9480
bii	B_S^2	Bulk	$0.0001 \to 0.9800$	0.6183(17)	1.780(109)	0.9819
bii	B_S^2	High	$0.9800 \to 0.9992$	0.2210(41)	104.2(2.1)	0.9829
bii	B_S^2	Extreme	$0.9992 \to 0.9999$	1.019(129)	$-819.7(166.1)$	0.9841
bii	B^2	Bulk	$0.0001 \to 0.9973$	0.6159(10)	1.870(85)	0.9935
bii	B^2	High	$0.9973 \to 0.9990$	1.420(152)	$-635.5(133.7)$	0.9606
bii	B^2	Extreme	$0.9990 \to 0.9999$	0.1282(190)	783.7(23.6)	0.9681
biii	B_S^2, cyc. 23	Bulk	$0.0001 \to 0.9913$	2.498(8)	$-12.61(28)$	0.9716
biii	B_S^2, cyc. 23	High	$0.9913 \to 0.9992$	8.236(238)	$-627.2(37.1)$	0.9838
biii	B_S^2, cyc. 23	Extreme	$0.9992 \to 0.9999$	1.396(220)	843.8(70.8)	0.9756
biii*	B^2, cyc. 23	Bulk	$0.0001 \to 0.9830$	2.274(7)	$-10.49(25)$	0.9751
biii*	B^2, cyc. 23	High	$0.9830 \to 0.9991$	6.572(121)	$-480.7(17.9)$	0.9863
biii	B^2, cyc. 23	Extreme	$0.9991 \to 0.9999$	2.450(373))	525.5(113.2)	0.9718
biii	B_S^2, cyc. 24	Bulk	$0.0001 \to 0.9825$	1.586(4)	2.036(102)	0.9842
biii	B_S^2, cyc. 24	High	$0.9825 \to 0.9991$	0.7953(78)	70.91(1.43)	0.9960
biii	B_S^2, cyc. 24	Extreme	$0.9991 \to 0.9999$	9.836(2.287)	$-3246(865)$	0.9366
biii*	B^2, cyc. 24	Bulk	$0.0001 \to 0.9975$	1.670(3)	1.716(91)	0.9928
biii	B^2, cyc. 24	High	$0.9975 \to 0.9990$	5.521(309)	$-975.4(89.9)$	0.9906

Panel	Parameter	PDF component	Fitting range	α	β	R^2
biii	B^2, cyc. 24	Extreme	$0.9990 \to 0.9999$	1.024(105)	563.7(38.8)	0.9845
ci	ϵ_S	Bulk	$0.0001 \to 0.9875$	0.9114(18)	$-0.0107(5)$	0.9900
ci	ϵ_S	High	$0.9875 \to 0.9996$	2.459(54)	$-1.852(91)$	0.9856
ci	ϵ_S	Extreme	$0.9996 \to 0.9999$	0.5839(3580)	4.896(1.461)	0.9610
cii	ϵ_S	All	$0.0001 \to 0.9999$	0.5014(8)	0.0147(7)	0.9942
ciii	ϵ_S, cyc. 23	Bulk	$0.0001 \to 0.9820$	2.295(6)	$-0.0286(15)$	0.9828
ciii	ϵ_S, cyc. 23	High	$0.9820 \to 0.9999$	4.807(88)	$-2.362(142)$	0.9850
ciii	ϵ_S, cyc. 24	Bulk	$0.0001 \to 0.9866$	2.357(7)	$-0.0350(17)$	0.9796
ciii	ϵ_S, cyc. 24	High	$0.9866 \to 0.9995$	0.8266(231)	0.7666(532)	0.9751
ciii	ϵ_S, cyc. 24	Extreme	$0.9995 \to 0.9999$	5.215(3.172)	$-28.42(22.52)$	0.9012
di	B_{z_S}	Bulk	$0.0001 \to 0.9914$	0.8763(8)	$-0.0796(20)$	0.9979
di	B_{z_S}	High	$0.9914 \to 0.9995$	1.489(14)	$-4.421(130)$	0.9983
di	B_{z_S}	Extreme	$0.9995 \to 0.9999$	0.3360(543)	9.931(817)	0.9923
dii	B_{z_S}	Bulk	$0.0001 \to 0.9785$	0.8606(5)	$-0.1038(16)$	0.9993
dii	B_{z_S}	High	$0.9785 \to 0.9995$	0.3027(69)	5.532(107)	0.9722
dii	B_{z_S}	Extreme	$0.9995 \to 0.9999$	2.513(552)	$-61.23(17.05)$	0.9859
diii	B_{z_S}, cyc.23	Bulk	$0.0001 \to 0.9910$	1.481(1)	0.0239(30)	0.9983
diii	B_{z_S}, cyc.23	High	$0.9910 \to 0.9995$	4.529(196)	$-23.08(1.84)$	0.9616
diii	B_{z_S}, cyc.23	Extreme	$0.9995 \to 0.9999$	0.2415(1314)	27.27(1.98)	0.9194
diii	B_{z_S}, cyc.24	Bulk	$0.0001 \to 0.9800$	1.455(1)	0.0320(13)	0.9995
diii	B_{z_S}, cyc.24	High	$0.9800 \to 0.9995$	0.8680(129)	3.181(104)	0.9891
diii	B_{z_S}, cyc.24	Extreme	$0.9995 \to 0.9999$	1.856(650)	$-11.38(9.72)$	0.9650
ei	$(v_x B_z)_S$	Bulk	$0.0001 \to 0.6500$	0.9017(6)	$-0.0140(3)$	0.9995
ei	$(v_x B_z)_S$	High	$0.6500 \to 0.9983$	1.104(1)	$-0.2246(20)$	0.9991
ei	$(v_x B_z)_S$	Extreme	$0.9983 \to 0.9999$	0.6214(411)	2.383(258)	0.9857
eii	$(v_x B_z)_S$	Bulk	$0.0001 \to 0.9626$	0.7358(5)	$-0.0422(8)$	0.9988
eii	$(v_x B_z)_S$	High	$0.9626 \to 0.9985$	0.2624(50)	1.870(33)	0.9670
eii	$(v_x B_z)_S$	Extreme	$0.9985 \to 0.9999$	1.280(92)	$-13.88(2.33)$	0.9611
eiii	$(v_x B_z)_S$, cyc.23	Bulk	$0.0001 \to 0.9920$	1.547(3)	0.0151(31)	0.9918
eiii	$(v_x B_z)_S$, cyc.23	High	$0.9920 \to 0.9976$	8.050(221)	$-23.03(91)$	0.9898
eiii	$(v_x B_z)_S$, cyc.23	Extreme	$0.9976 \to 0.9999$	1.142(72)	9.256(426)	0.9800
eiii	$(v_x B_z)_S$, cyc.24	Bulk	$0.0001 \to 0.7600$	1.198(1)	0.0187(7)	0.9982
eiii	$(v_x B_z)_S$, cyc.24	High	$0.7600 \to 0.9994$	0.9706(27)	0.2451(57)	0.9952
eiii	$(v_x B_z)_S$, cyc.24	Extreme	$0.9994 \to 0.9999$	3.136(1.510)	$-13.21(9.21)$	0.9147

Table S2: Fit parameters for the linear regressions shown by the black dashed lines in figure S1, in same format as table S1.

Panel	Parameter	PDF component	Fitting range	α	β	R^2
ai	v_S	Bulk	$0.0001 \to 0.7600$	1.943(4)	$-338.5(1.5)$	0.9926
ai	v_S	High	$0.8528 \to 0.9999$	0.8150(29)	193.3(1.5)	0.9926
aii	v_S	Bulk	$0.0001 \to 0.9155$	0.6466(8)	85.67(32)	0.9970
aii	v_S	High	$0.9155 \to 0.9990$	1.081(5)	$-171.6(3.1)$	0.9958
aii	v_S	Extreme	$0.9990 \to 0.9999$	3.858(909)	$-2364(728)$	0.9230
aiii	v_S, cyc. 23	Bulk	$0.0001 \to 0.9970$	1.256(1)	$-80.21(52)$	0.9976
aiii	v_S, cyc. 23	High	$0.9970 \to 0.9999$	0.4469(360)	479.1(25.1)	0.9584
aiii	v_S, cyc. 24	Bulk	$0.0001 \to 0.8870$	0.4610(9)	158.4(4)	0.9909
aiii	v_S, cyc. 24	High	$0.8870 \to 0.9999$	1.838(9)	$-700.0(5.9)$	0.9933
bi	$\sin^4(\theta/2)$	Bulk	$0.0001 \to 0.8660$	1.053(1)	$-9.266(206) \times 10^{-4}$	0.9998
bi	$\sin^4(\theta/2)$	High	$0.8660 \to 0.9999$	0.8995(6)	0.0251(2)	0.9998
bii	$\sin^4(\theta/2)$	All	$0.0001 \to 0.9999$	1.017(1)	$6.664(346) \times 10^{-4}$	0.9997
biii	$\sin^4(\theta/2)$, cyc.23	All	$0.0001 \to 0.9999$	1.012(1)	$-0.0012(1)$	0.9998
biii	$\sin^4(\theta/2)$, cyc.24	All	$0.0001 \to 0.9999$	0.9995(1)	$-4.540(110) \times 10^{-4}$	1.0000

ci	$B^2_{x,S}$	Bulk	$0.0001 \to 0.9450$	0.8333(10)	$-0.1471(100)$	0.9969
ci	$B^2_{x,S}$	High	$0.9450 \to 0.9988$	1.653(15)	$-24.35(62)$	0.9888
ci	$B^2_{x,S}$	Extreme	$0.9988 \to 0.9999$	0.8435(1493)	47.01(14.36)	0.9407
cii	$B^2_{x,S}$	Bulk	$0.0001 \to 0.9920$	0.5762(5)	0.1200(117)	0.9982
cii	$B^2_{x,S}$	High	$0.9920 \to 0.9996$	0.6226(246)	$-19.66(4.95)$	0.9713
cii	$B^2_{x,S}$	Extreme	$0.9996 \to 0.9999$	0.0602(408)	212.0(21.5)	0.9527
ciii	$B^2_{x,S}$, cyc. 23	Bulk	$0.0001 \to 0.8860$	1.608(1)	$-0.1037(83)$	0.9992
ciii	$B^2_{x,S}$, cyc. 23	High	$0.8860 \to 0.9935$	2.654(11)	$-22.88(35)$	0.9954
ciii	$B^2_{x,S}$, cyc. 23	Extreme	$0.9935 \to 0.9999$	6.218(163)	$-203.9(11.4)$	0.9893
ciii	$B^2_{x,S}$, cyc. 24	Bulk	$0.0001 \to 0.9960$	1.145(1)	0.1602(185)	0.9958
ciii	$B^2_{x,S}$, cyc. 24	High	$0.9960 \to 0.9996$	2.916(120)	$-154.1(11.7)$	0.9859
ciii	$B^2_{x,S}$, cyc. 24	Extreme	$0.9996 \to 0.9999$	0.5579(1273)	161.1(18.8)	0.9944
di	$B^2_{yz,S}$	Bulk	$0.0001 \to 0.9500$	0.7263(8)	$-0.3895(148)$	0.9970
di	$B^2_{yz,S}$	High	$0.9500 \to 0.9992$	1.827(29)	$-67.84(2.55)$	0.9688
di	$B^2_{yz,S}$	Extreme	$0.9992 \to 0.9999$	0.2258(686)	307.5(20.0)	0.9154
dii	$B^2_{yz,S}$	Bulk	$0.0001 \to 0.9850$	0.6548(10)	0.9849(519)	0.9937
dii	$B^2_{yz,S}$	High	$0.9850 \to 0.9991$	0.2264(29)	88.96(1.34)	0.9942
dii	$B^2_{yz,S}$	Extreme	$0.9991 \to 0.9999$	1.502(204)	$-1083(203)$	0.9774
diii	$B^2_{yz,S}$, cyc. 23	Bulk	$0.0001 \to 0.9860$	2.329(5)	$-2.469(119)$	0.9870
diii	$B^2_{yz,S}$, cyc. 23	High	$0.9860 \to 0.9986$	7.879(168)	$-494.0(19.8)$	0.9858
diii	$B^2_{yz,S}$, cyc. 23	Extreme	$0.9986 \to 0.9999$	1.156(173)	665.2(43.9)	0.9464
diii	$B^2_{yz,S}$, cyc. 24	Bulk	$0.0001 \to 0.9770$	1.932(3)	1.518(54)	0.9920
diii	$B^2_{yz,S}$, cyc. 24	High	$0.9770 \to 0.9992$	0.7258(131)	79.75(1.75)	0.9818
diii	$B^2_{yz,S}$, cyc. 24	Extreme	$0.9992 \to 0.9999$	5.591(2.53)	$-1658(942)$	0.8297
ei	$\phi_{D,S}$	Bulk	$0.0001 \to 0.9964$	1.036(2)	$-0.4615(135)$	0.9933
ei	$\phi_{D,S}$	High	$0.9964 \to 0.9995$	2.717(152)	$-48.91(5.31)$	0.9780
ei	$\phi_{D,S}$	Extreme	$0.9995 \to 0.9999$	0.5654(3312)	45.12(15.38)	0.9077
eii	$\phi_{D,S}$	Bulk	$0.0001 \to 0.9300$	0.7147(3)	$-0.0705(24)$	0.9997
eii	$\phi_{D,S}$	High	$0.9300 \to 0.9995$	0.6061(13)	2.633(51)	0.9992
eii	$\phi_{D,S}$	Extreme	$0.9995 \to 0.9999$	1.470(486)	$-80.51(53.95)$	0.9686
eiii	$\phi_{D,S}$, cyc. 23	Bulk	$0.0001 \to 0.9246$	1.525(1)	$1.393(16.75) \times 10^{-4}$	0.9999
eiii	$\phi_{D,S}$, cyc. 23	High	$0.9246 \to 0.9962$	2.407(5)	$-13.57(11)$	0.9991
eiii	$\phi_{D,S}$, cyc. 23	Extreme	$0.9962 \to 0.9999$	3.024(82)	$-29.37(2.99)$	0.9935
eiii	$\phi_{D,S}$, cyc. 24	Bulk	$0.0001 \to 0.9970$	1.118(1)	0.1794(40)	0.9995
eiii	$\phi_{D,S}$, cyc. 24	High	$0.9970 \to 0.9995$	0.6503(449)	18.80(2.17)	0.9739
eiii	$\phi_{D,S}$, cyc. 24	Extreme	$0.9995 \to 0.9999$	7.036(2.741)	$-419.7(195.5)$	0.9570
fi	$(d\phi/dt)_S$	Bulk	$0.0001 \to 0.8000$	1.018(1)	$-18.97(45)$	0.9994
fi	$(d\phi/dt)_S$	High	$0.8000 \to 0.9999$	1.324(2)	$-564.5(5.1)$	0.9991
fii	$(d\phi/dt)_S$	Bulk	$0.0001 \to 0.9986$	0.7040(3)	6.565(561)	0.9997
fii	$(d\phi/dt)_S$	High	$0.9986 \to 0.9999$	1.056(55)	$-4597(738)$	0.9931
fiii	$(d\phi/dt)_S$, cyc. 23	Bulk	$0.0001 \to 0.9400$	1.426(1)	$-28.25(57)$	0.9997
fiii	$(d\phi/dt)_S$, cyc. 23	High	$0.9400 \to 0.9973$	1.954(2)	$-1542(9)$	0.9998
fiii	$(d\phi/dt)_S$, cyc. 23	Extreme	$0.9973 \to 0.9999$	3.619(81)	$-1.095(50) \times 10^4$	0.9971
fiii	$(d\phi/dt)_S$, cyc. 24	Bulk	$0.0001 \to 0.9990$	0.9291(7)	29.94(1.17)	0.9985
fiii	$(d\phi/dt)_S$, cyc. 24	High	$0.9990 \to 0.9999$	3.246(504)	$-1.824(440) \times 10^4$	0.9650

Table S3: Fit parameters for the linear regressions shown by the black dashed lines in figure S2, in same format as table S1.

Panel	Parameter	PDF component	Fitting range	α	β	R^2
a	S_S	Bulk	$0.0001 \rightarrow 0.9972$	$0.5867(6)$	$2.498(132) \times 10^{-4}$	0.9971
a	S_S	High	$0.9972 \rightarrow 0.9999$	$0.3616(79)$	$0.0423(38)$	0.9971
a*	S	Bulk	$0.0001 \rightarrow 0.9972$	$0.5948(8)$	$2.077(186) \times 10^{-4}$	0.9945
a	S	High	$0.9972 \rightarrow 0.9999$	$0.2904(72)$	$0.0510(37)$	0.9962
b	B_S^2	Bulk	$0.0001 \rightarrow 0.9980$	$0.6582(3)$	$-0.9130(231)$	0.9995
b	B_S^2	High	$0.9980 \rightarrow 0.9999$	$0.4057(223)$	$181.9(27.5)$	0.9878
b*	B^2	Bulk	$0.0001 \rightarrow 0.9980$	$0.6749(5)$	$-0.8351(398)$	0.9984
b	B^2	High	$0.9980 \rightarrow 0.9999$	$0.3373(266)$	$270.7(32.6)$	0.9752
c	ϵ_S	Bulk	$0.0001 \rightarrow 0.9970$	$0.6152(4)$	$-0.0031(3)$	0.9990
c	ϵ_S	High	$0.9970 \rightarrow 0.9999$	$0.4359(116)$	$0.9469(1373)$	0.9953
d	$(v_x B_z)_S$	Bulk	$0.0001 \rightarrow 0.9975$	$0.7636(5)$	$-0.0027(8)$	0.9989
d	$(v_x B_z)_S$	High	$0.9975 \rightarrow 0.9999$	$0.4303(187)$	$2.812(293)$	0.9900
e	$B_{z,S}$	Bulk	$0.0001 \rightarrow 0.9975$	$0.8348(4)$	$-0.0663(15)$	0.9994
e	$B_{z,S}$	High	$0.9975 \rightarrow 0.9999$	$0.3237(139)$	$9.387(335)$	0.9901
f	v_S	Bulk	$0.0001 \rightarrow 0.9500$	$0.9980(8)$	$-21.85(31)$	0.9987
f	v_S	High	$0.9500 \rightarrow 0.9996$	$0.6136(24)$	$228.4(1.6)$	0.9982
f	v_S	Extreme	$0.9996 \rightarrow 0.9999$	$1.079(639)$	$-234.4(625.3)$	0.9635
g	$(d\phi/dt)_S$	Bulk	$0.0001 \rightarrow 0.9945$	$0.8040(2)$	$-17.30(44)$	0.9998
g	$(d\phi/dt)_S$	High	$0.9945 \rightarrow 0.9999$	$0.5795(68)$	$1515(73)$	0.9982
h	$\phi_{D,S}$	Bulk	$0.0001 \rightarrow 0.9920$	$0.7635(3)$	$-0.1240(15)$	0.9998
h	$\phi_{D,S}$	High	$0.9920 \rightarrow 0.9999$	$0.5572(44)$	$9.394(310)$	0.9988